Supplementary Information for

Magnetoelastoresistance in WTe_2

Na Hyun Jo, Lin-Lin Wang, Peter P. Orth, Sergey L. Bud'ko and Paul C. Canfield

Na Hyun Jo.
E-mail: njo@iastate.edu,
Paul C. Canfield.
E-mail: canfield@ameslab.gov

This PDF file includes:

Supplementary text
Figs. S1 to S10
Table S1
References for SI reference citations

Supporting Information Text

1. Elastoresistance tensor and Gauge factor

The elastoresistance of a material characterizes the changes of the resistance of the material due to the stress experienced by the material. Based on the definition of resistance, $R = \rho\frac{L}{A}$, changes in the resistance can be written as

$$\frac{dR}{R} = \frac{d\rho}{\rho} + \frac{dL}{L} - \frac{dA}{A}. \quad [1]$$

The first term is the change in the resistivity of the material which relates to the electronic properties of the material. The second and the third terms are purely geometrical factors. For typical metals, such as Cu, these geometric terms dominate elastoresistance. However, strain dependent changes in density of states, mobility, scattering, etc. (elastoresistivity) play important roles in cases like WTe_2.

The elastoresistivity is described by

$$(\frac{d\rho}{\rho})_i = \sum_{k=1}^{6} m_{ik}\varepsilon_k \quad [2]$$

where m_{ik} is the elastoresistive strain matrix and ε_k is the strain tensor in Voigt notation. (1) For an orthorhombic structure, there are nine independent terms in the elastoresistivity tensor: (2)

$$\begin{pmatrix} m_{11} & m_{12} & m_{13} & 0 & 0 & 0 \\ m_{12} & m_{22} & m_{23} & 0 & 0 & 0 \\ m_{13} & m_{23} & m_{33} & 0 & 0 & 0 \\ 0 & 0 & 0 & m_{44} & 0 & 0 \\ 0 & 0 & 0 & 0 & m_{55} & 0 \\ 0 & 0 & 0 & 0 & 0 & m_{66} \end{pmatrix}. \quad [3]$$

Considering our measurement configuration, the stress was applied only along the crystallographic a direction, the stress is

$$\tau = (\tau_{xx}, \tau_{yy}, \tau_{zz}, \tau_{yz}, \tau_{zx}, \tau_{xy}) = (\tau_{xx}, 0, 0, 0, 0, 0). \quad [4]$$

Since the stain ε can be expressed in terms of the elastic compliance S and the stress τ,

$$\varepsilon_k = \sum_{l=1}^{6} S_{kl}\tau_l, \quad [5]$$

the strain therefore is:

$$\varepsilon = (\varepsilon_{xx}, \varepsilon_{yy}, \varepsilon_{zz}, 0, 0, 0). \quad [6]$$

If we neglect geometric factors, the change in resistance of the crystal is given by

$$(\frac{dR}{R})_{xx} = m_{11}\varepsilon_{xx} + m_{12}\varepsilon_{yy} + m_{13}\varepsilon_{zz} \quad [7]$$

The strain terms in the y and z directions are determined by the Poisson's ratio of the crystal, ν_{xy} and ν_{xz}.

$$(\frac{dR}{R})_{xx} = \varepsilon_{xx}(m_{11} + \nu_{xy}m_{12} + \nu_{xz}m_{13}). \quad [8]$$

The Gauge factor (GF) can also be obtained from Eq. (1):

$$GF = (\frac{(dR/R)_{xx}}{\varepsilon_{xx}}) = \frac{(d\rho/\rho)_{xx}}{\varepsilon_{xx}} + (1 + 2\nu). \quad [9]$$

The GF of ordinary metals, like copper, is a temperature independent value with magnitude around 2. This is because geometric factor is the dominant term and Poisson's ratio for the most of metals is $0.3 < \nu < 0.5$. (3) A recent paper on WTe_2 calculated the Poisson's ratio ν of the material as $\nu \sim 0.16$. (4, 5) Since we obtained GFs much larger than 2, and, at times, with negative signs, for WTe_2, changes in the electronic properties rather than geometry, are dominant. Therefore, measurements of elastoresistivity (and its response to magnetic field) offer new insight into the electronic properties of WTe_2.

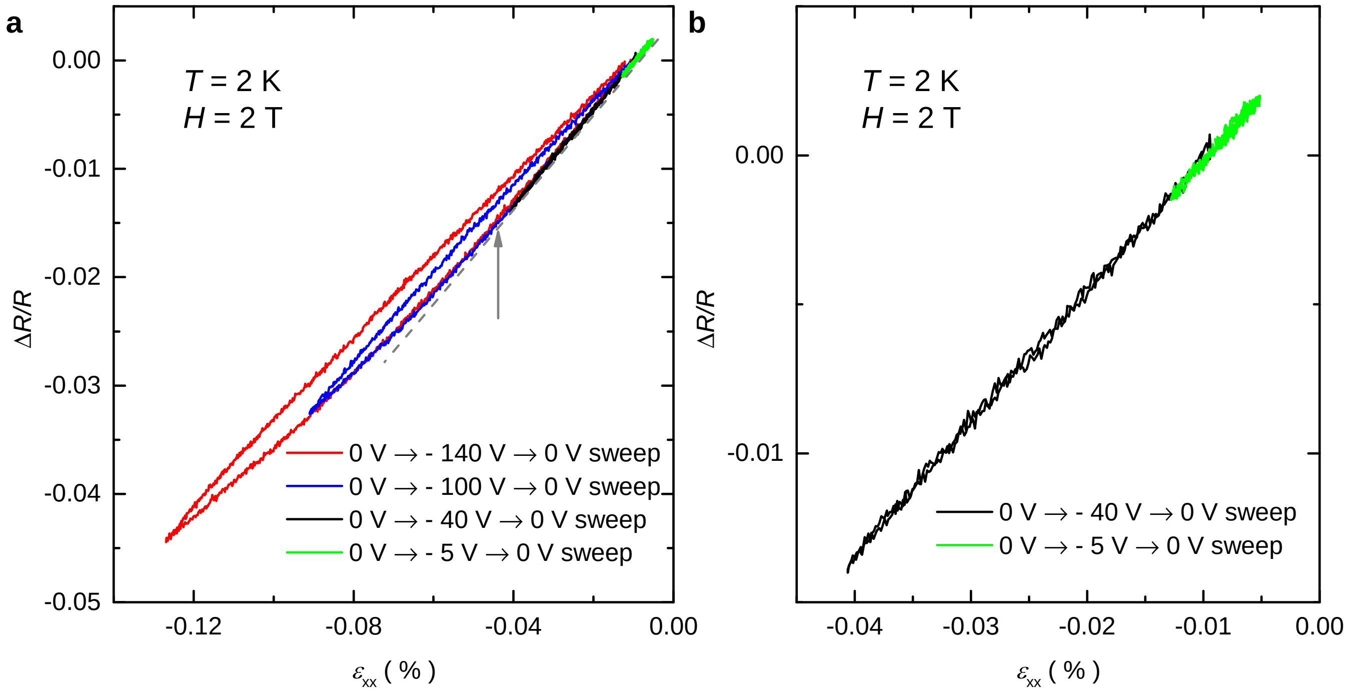

Fig. S1. a, Resistance response to the strain with various voltage limits Strain(ε_{xx}) sweep at fixed temperature of $T = 2\,\mathrm{K}$ and the magnetic field $H = 2\,\mathrm{T}$ with various voltage limits; -5 V (green line), -40 V (black line), -100 V (blue line) and -140 V (red line). The green dashed line is a guide line to point out the deviation from linear behavior, which also indicated with the gray arrow. **b**, 0 V → -5 V → 0 V, and 0 V → -40 V → 0 V sweeps on an expanded scale.

2. Methods

Single crystals of $\mathrm{WTe_2}$ were grown out of a Te-rich, binary melt, following the procedure described in Ref. (6). Temperature and field dependent transport properties were measured in a Quantum Design(QD), Physical Property Measurement System for $1.8 \leq \mathrm{T} \leq 300\,\mathrm{K}$ and $|H| \leq 140\,\mathrm{kOe}$. Resistance measurements under uniaxial stress were carried out using a Razorbill CS100 cryogenic uniaxial stress cell. To be more specific, outer and inner piezoelectric stacks were controlled by two Keithley Model 2400 source meters, and corresponding length changes of the crystals were measured by a capacitance sensor using an Andeen-Hagerling(AH) Model 2550A capacitance bridge. Note that there is always certain errors in the length change measurements due to thermal contraction of various parts. Although some thermal effects were addressed (i.e. the thermal effect from piezoelectric materials was canceled via symmetric usage of outer and inner piezoelectric stacks and the thermal effect from the capacitance sensor was removed by subtracting the temperature dependence capacitance of the empty cell result), others, including the thermal contraction from the cell and the crystal itself, were not considered. The crystals were mounted across the two plates with Stycast 2850 FT, so that the crystal was mechanically attached to the plates firmly and electrically isolated from the cell body.(Fig.1 a) We estimated that, due to the epoxy, about 80 % of the displacement was transmitted as sample strain. In this calculation, we used the Young's modulus of the crystals of 80 GPa and the thickness of the glue was $\sim 50\,\mu m$. (5, 7) The contacts for the electrical transport measurement were prepared in a standard linear four-probe configuration using Epotek-H20E silver epoxy and silver paint, and Lakeshore Model 370 AC resistance bridge was used for the resistance measurement of the crystals. Due to the large drop in the resistivity of $\mathrm{WTe_2}$ upon cooling in zero field, combined with the limit of the resistance bridge (resolution is $1\,\mu\Omega$ with $I = 3.16\,\mathrm{mA}$ in the range of $2.0\,\mathrm{m}\Omega$), we were not able to conduct the elastoresistance measurements below $T < 50\,\mathrm{K}$ with $H = 0\,\mathrm{T}$ in the above experimental setting. In order to overcome this limit of the measurement, we performed the elastoresistance experiment without the magnetic field using Stanford Research Systems(SRS) 860, Lock-In Amplifier and SRS Model CS580, voltage controlled current source in a Janis SHI-950-T closed cycle cryostat. Two samples were measured in this way, S3' and S4. S3' is esentially same as S3, which was measured in PPMS, but new contacts were made after cleaving the top layer. S4 was mounted in a Razorbill CS130 cryogenic uniaxial stress cell. S4 was secured with a small amount of Devcon 5 minute epoxy in between anodized plates, which can give the largest transmitted strain on the sample.

As we applied uniaxial stress along the crystallographic a axis, three strain tensor components are non-zero in Voigt notation. (see SI) However, we measured only one component, ε_{xx}, due to the experimental set up. In this paper, we define strain as $\varepsilon_{xx}\,[\%] = [(L - L_0)/L_0] \times 100$, where L_0 is the unstrained length. Thus, a positive sign represents tensile strain and a negative sign stands for compressive strain. We noticed that the crystals are very easy to break when even a small amount of tensile strain is applied. The compressive strain at which the sample starts to buckle can be calculated based on the ratio between length and thickness (L/t) of the crystals: $L/t = \pi/\sqrt{3\varepsilon_{xx}}$. (8) From the calculation, we expected buckling of all three samples that we measured above $\varepsilon_{xx} = -1.5\,\%$. However, the first sample of $\mathrm{WTe_2}$, S1, cleaved at $\varepsilon_{xx} \sim -0.3\,\%$, which was before the sample started to buckle due to the easily exfoliatable nature of the crystal. In addition, the second crystal, S2, showed a jump at $\varepsilon_{xx} \sim -0.16\,\%$ without visual observation of a cleave or crack in the sample. This might indicate that cracks or small cleaving can happen even with small strain due to the layered structure. Based on all of the above, elastoresistance measurements were done only $\varepsilon_{xx} \leq \pm 0.013\,\%$ which corresponds to a maximum voltage applied to the piezoelectric material of $V = \pm 5\,\mathrm{V}$ for the third single crystals of $\mathrm{WTe_2}$, S3. Within this range, resistance response to the strain ($\Delta R/R$ vs. strain) was linear without hysteresis (more details are in SI). Details about Shubnikov de Haas oscillations can be found in SI.

Band structures of $\mathrm{WTe_2}$ at strains from 0 to -0.2 % were calculated in density functional theory (9, 10) (DFT) using local density approximation (11, 12) (LDA) with spin-orbit coupling (SOC) effect included. The dimensions of the unit cells were determined from experimental lattice constants (13) ($a = 3.477$ Å, $b = 6.249$ Å and $c = 14.018$ Å) plus strain and a Poisson ratio (4) of 0.16. The ionic positions in the unit cells were relaxed at different strains and then band structures are calculated. The band structure with relaxed ionic positions at this strain range is insensitive to the out-of-plane strain because of the weak vdW interaction and large spacing between the stacking layers along *c*-axis. The carrier densities were calculated from the volume of electron and hole pockets in reciprocal space. The quantum oscillation frequencies were calculated by finding the extreme orbit (14) of hole and electron pockets with the magnetic field along the *c* direction. The conductivity without magnetic field were calculated from the semi-classical Boltzmann equation with the interpolated DFT band structures. (15) DFT calculations were done in VASP (16) with a plane-wave basis set and projector augmented wave (17) method. We used the orthorhombic cell of 12 atoms with a Γ-centered Monkhorst-Pack (18) $(12 \times 6 \times 3)$ *k*-point mesh. The kinetic energy cutoff was 223 eV. The convergence with respect to *k*-point mesh was carefully checked, with total energy converged, e.g., well below 1 meV/atom. For ionic relaxation, the absolute magnitude of force on each atom was reduced below 0.01 eV Å.

3. Elastoresistance experiment

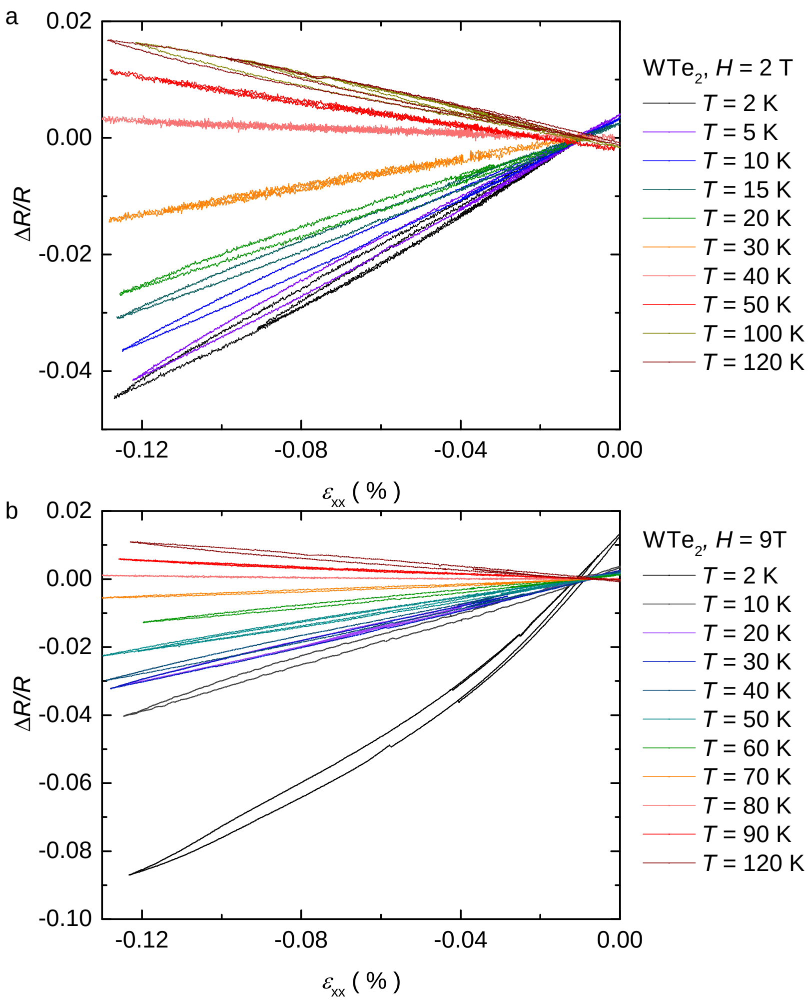

Fig. S2. Resistance response to the strain with various temperatures a, Strain(ε_{xx}) sweeps in the magnetic field of 2 T. **b**, Strain(ε_{xx}) sweeps in the magnetic field of 9 T. Note: clear non-linearity in 2 K data is likely associated with strain induced changes in Quantum oscillation (QO) frequencies and QO in Magneto-elastoresistance (MER) is discussed below.

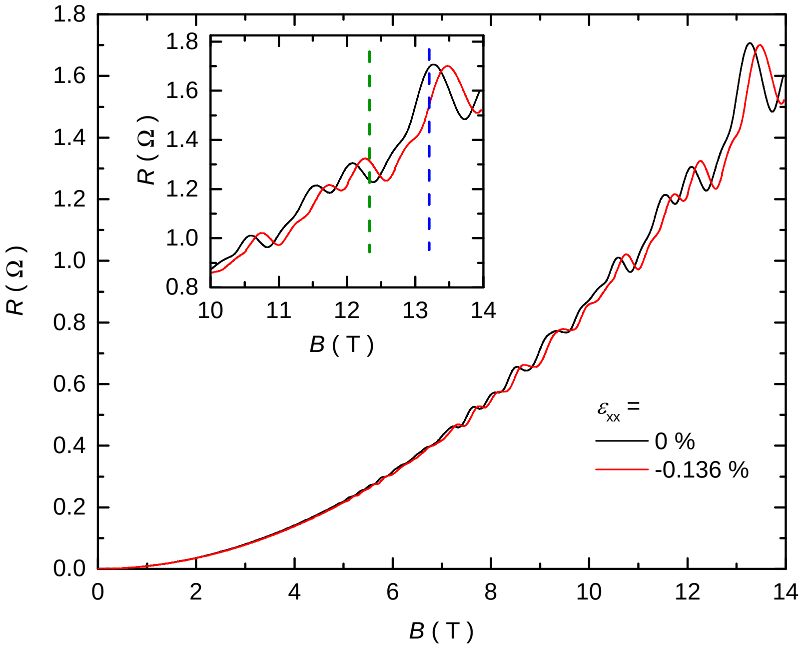

Fig. S3. Large changes in elastoresistance Magnetoresistance data without(black line, $\varepsilon_{xx} = 0\,\%$) strain and with (red line, $\varepsilon_{xx} = -0.136\,\%$) strain at $T = 2$ K. Inset shows magnetoresistances from 10 T to 14 T on an enlarged scale.

We took care to measure our data in the linear response limit. To do this we measured $\Delta R/R$, where $\Delta R = R(\varepsilon_{xx}) - R(\varepsilon_{xx} = 0)$, versus strain loops for a variety of strain (or voltage) sweeps at base temperature (Fig. S1) as well as over the whole temperature range (Fig S2). We find that as we increase the size of strain sweeps there is an increasing hysteresis. As a result of these measurements and out of an abundance of caution, we limit our measurements of ER to a maximum voltage applied to the piezoelectric material of $V = \pm 5\,$V, which correspond to $|\varepsilon_{xx}| \leq 0.013\,\%$ for sample S3, so as to be in the linear regime (See Fig. S1). On the other hand, quantum oscillation analyses with applied strain were limited to $|\varepsilon_{xx}| \leq 0.136\,\%$. In this range, the shift in quantum oscillations frequency is linear as shown in Fig. 3 e, although there was hysteresis in the $\Delta R/R$ versus strain data. We also performed experiments on various samples to check reproducibility. S1 was the first sample, that was cleaved due to applying too much strain. Here, ER was unrepeatable with a non-linear big hysteresis. S2 was the second sample that we show in the manuscript. The same experiments on the third sample, S3, were performed to confirm the result from S2. S3' is basically same as S3, but the a few top layers were cleaved to redo the electrical contacts. The experiments on S4 were conducted to check the low temperature data in zero the magnetic field on S3'.

4. Large changes in elastoresistance due to quantum oscillations

Figure S3 shows the low-temperature magnetoresistance (MR) without strain ($\varepsilon_{xx} = 0$) and with a strain of $\varepsilon_{xx} = -0.136\,\%$ at $T = 2\,$K. Whereas the MR increases quadratically without saturation up to 14 T, quantum oscillations are detected above $\sim 4\,$T in both cases. Due to the strain induced changes in frequencies, there are mismatches in the quantum oscillation peaks in the high magnetic field regime. Therefore, the elastoresistance (ER) change dramatically from negative to positive with small changes of the magnetic field. To illustrate this more clearly, we focus on MR from 10 T to 14 T in the inset of Fig. S3. The vertical green dashed line indicates a negative ER whereas the blue dashed line indicates a positive ER.

Subtracting the MR without strain from MR with strain allows us to directly examine the oscillations in the magneto-elastoresistance (MER). This is shown in Fig. S4a and c. In order to corroborate these as quantum oscillations, we perform a fast Fourier transform (FFT) on the data as a function of $1/B$. Figure S4b and d are the results of FFT on S2 and S3. All four frequencies, that were detected from SdH measurements, are observed in both samples. As such, these data, as well as the data highlighted in the inset of Fig. 2a and b, are clear manifestations of quantum oscillations in MER.

To further investigate these MER quantum oscillations, we use Lifshitz and Kosevich theory to arrive at

$$\Delta_\varepsilon R = \sum_i A_i(B,T) \left[\sin\left(\frac{2\pi[F_i + \delta F_i(\varepsilon_{xx})]}{B} + \phi_i \right) - \sin\left(\frac{2\pi F_i}{B} + \phi_i \right) \right] , \qquad [10]$$

where $\Delta_\varepsilon R \equiv R(\varepsilon_{xx} \neq 0) - R(\varepsilon_{xx} = 0)$ and $\delta F_i(\varepsilon_{xx})$ denotes the shift of frequencies due to strain. As noted above, this shift is due to a strain-induced change of the bandstructure, resulting in a change of the size of the extremal orbit. Note that in Eq. (10) we have neglected the change of the quadratic background part of MR under strain, which is subleading. We also assume that ϕ_i and A_i are independent of strain.

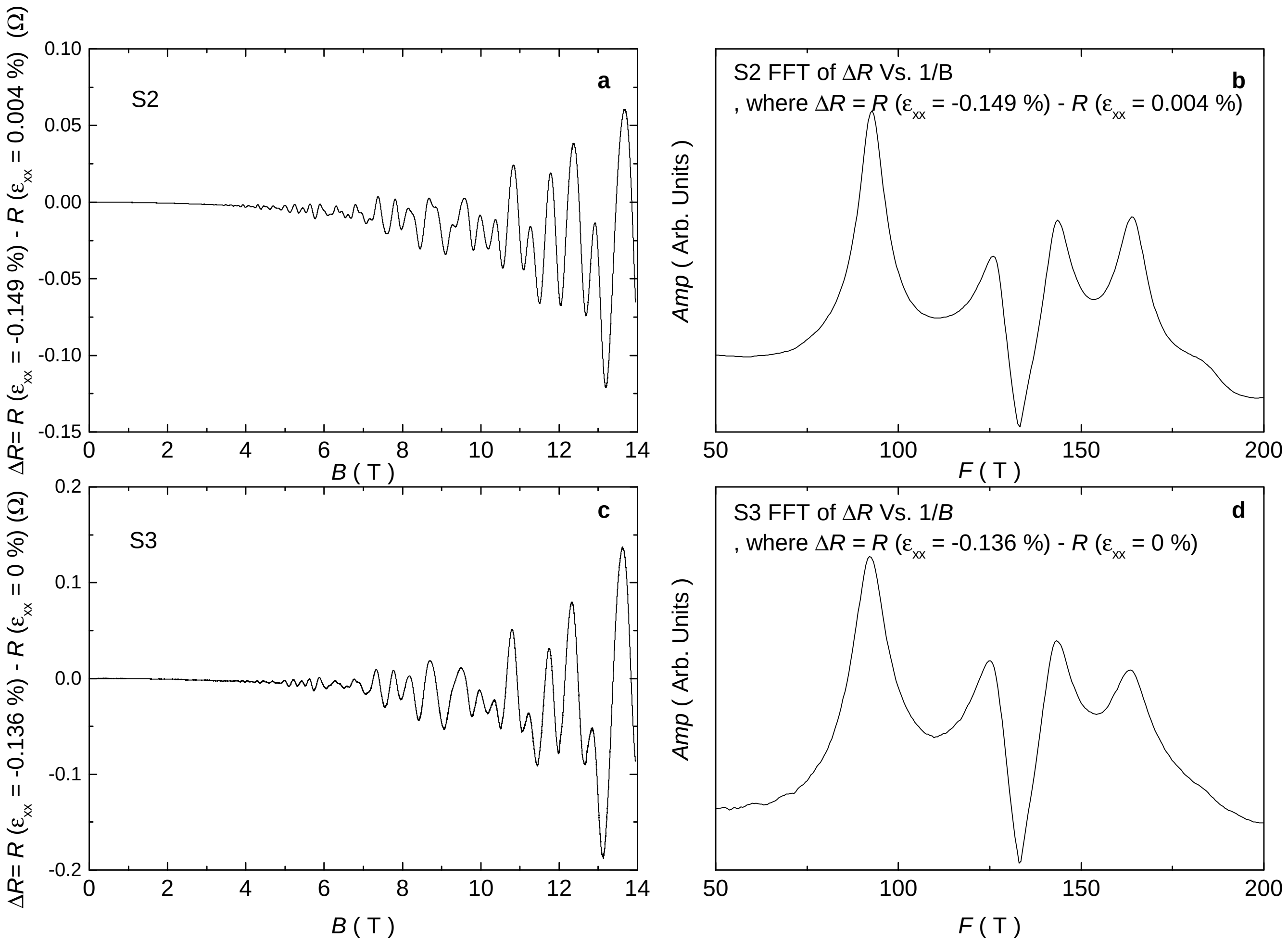

Fig. S4. QO in MER a, $\Delta R = R(\varepsilon_{xx} = -0.149\,\%) - R(\varepsilon_{xx} = 0.004\,\%)$ as a function of the magnetic field in S2. **b**, FFT of ΔR in terms of $1/B$ in S2. **c**, $\Delta R = R(\varepsilon_{xx} = -0.136\,\%) - R(\varepsilon_{xx} = 0\,\%)$ as a function of the magnetic field in S3. **d**, FFT of ΔR in terms of $1/B$ in S3.

For small strain one finds $\delta F/F \propto \varepsilon_{xx} \ll 1$ such that Eq. (10) becomes

$$\Delta_\varepsilon R = \sum_i A_i(B,T)\cos\left(\frac{2\pi F_i}{B} + \phi_i\right)\frac{2\pi\delta F_i(\varepsilon_{xx})}{B}\,. \qquad [11]$$

The important conclusion is that the frequencies of the MER oscillations in $\Delta_\varepsilon R$ are identical to the frequencies observed in SdH oscillations of the MR.

5. Quantum oscillation analysis

When using a fast Fourier transformation (FFT) to determine the frequencies of the quantum oscillations, the frequency resolution is generally determined by the size of the Fourier window. Figure S5 highlights the data spacing around the local maximum which defines F^1; the data points are more closely spaced for wider field range windows. In order to resolve the strain dependence of frequency changes in WTe$_2$, within a relatively small strain range, the magnetic field range of $0.5\,\mathrm{T} < H < 13.95\,\mathrm{T}$ was used for all strains. In order to check the reproducibility of these results, we performed similar experiments and analysis on sample S3 with a fewer number of strains. As shown in Fig. S6a and b, S3 also shows similar behavior as S2 (Fig. 3).

Although the resolution is important to resolve the peaks, one is also interested in analyzing the amplitude of the peaks to obtain the associated effective masses. In this case, it is important to choose a magnetic field range that starts at the field strength where the MR begins to show quantum oscillations at the highest temperature. To be more specific, the amplitude of peaks can be reduced due to an artifact of the FFT analysis which comes from including low magnetic field MR data into the Fourier window, where MR does not exhibit quantum oscillations at higher temperatures. In addition, quantum oscillations at higher temperatures require higher magnetic fields to start. Thus, one needs to determine the magnetic field range based on the highest temperature data that will be used for the analysis. Taking this into account we used a magnetic field range of $5\,\mathrm{T} < H < 13.95\,\mathrm{T}$ to infer the amplitude changes as a function of the temperature with different strains.

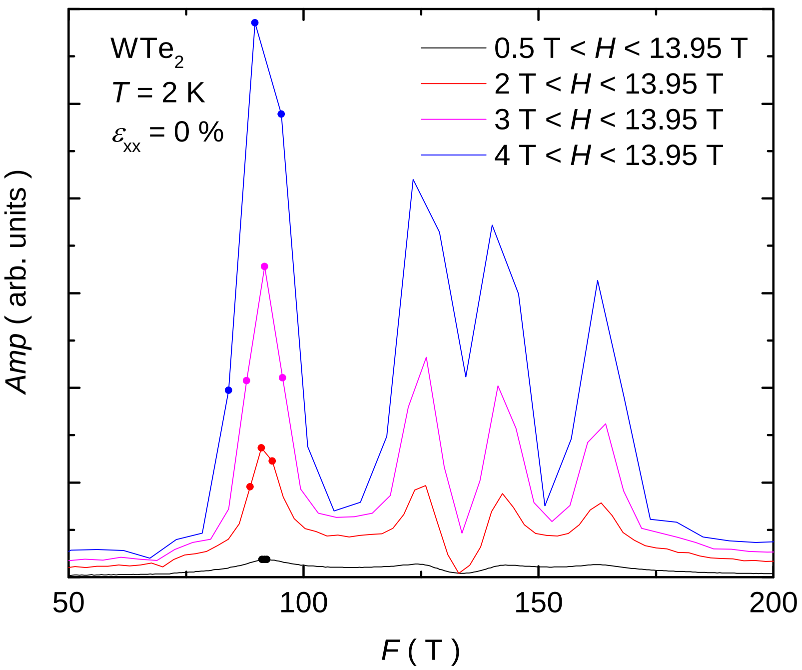

Fig. S5. Resolution of frequencies FFT results of WTe$_2$ at $T = 2$ K and $\varepsilon_{xx} = 0\,\%$ for various magnetic field ranges. The filled circles are the data point at F^1 and the nearest data points around the F^1.

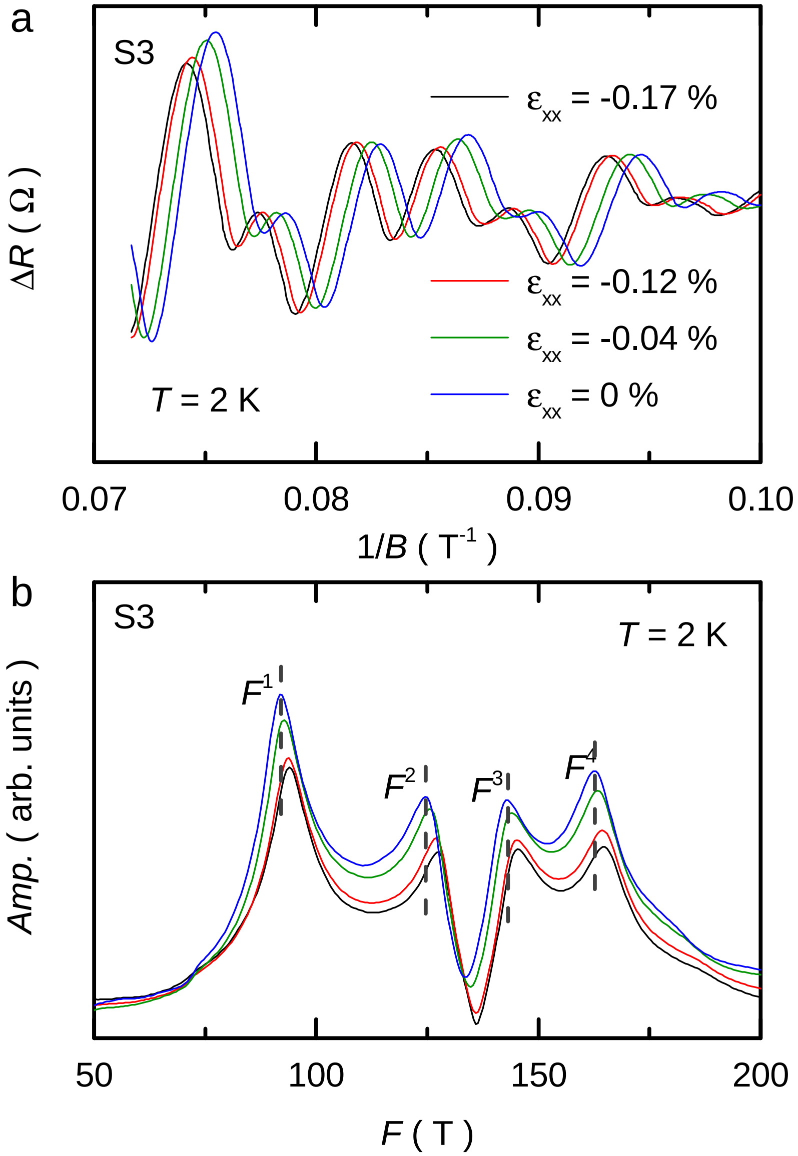

Fig. S6. Confirmation of the frequency changes with strain a, SdH oscillations at various strains for S3. **b**, FFT results at various strains, and gray dashed lines are the position of the local maximum for $\varepsilon_{xx} = 0\,\%$ and serve as guide lines for the shifting of the frequencies.

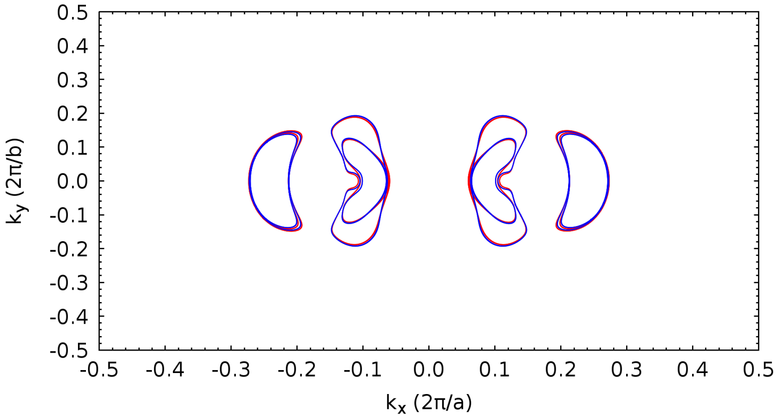

Fig. S7. DFT calculation of Fermi surface Full brillouin zone Fermi surface calculation results from DFT for strain (ε_{xx}) at 0 (blue line) and -0.2 % (red line).

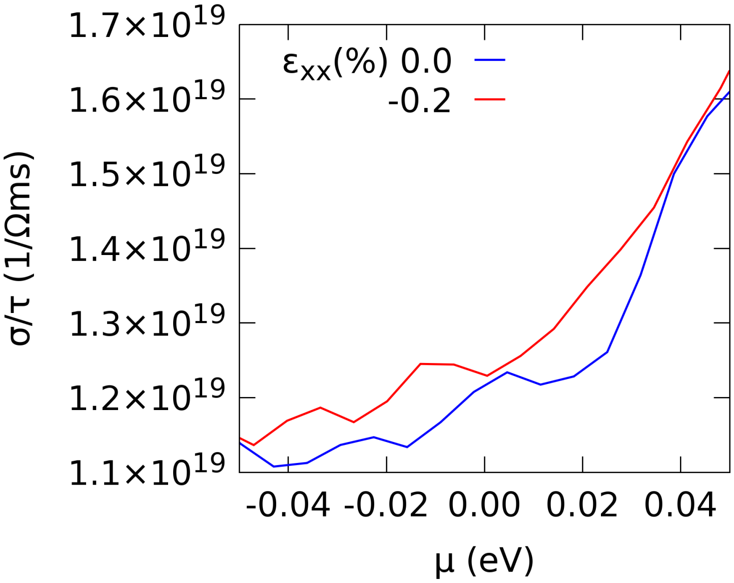

Fig. S8. DFT calculation of Conductivity as a function of chemical potential Conductivity over relaxation time (σ/τ) vs. electronic chemical potential (μ) as calculated from semi-classical Boltzmann model with DFT band structure for strain (ε_{xx}) at 0 (blue line) and -0.2 % (red line).

6. Full Brillouin zone from density functional theory (DFT) calculations

7. Electrical conductivity from DFT calculations

The conductivity is calculated from the semi-classical Boltzmann equation with the interpolated DFT band structures at $T = 0\,\mathrm{K}$ (15). The ratio of conductivity and relaxation time σ/τ without and with applied strain ε_{xx} = -0.2 % is plotted as a function of chemical potential in Fig. S8. We find a positive elastoresistance (ER), i.e., for negative strain the conductivity goes up, within the chemical potential range of -0.04 < μ < 0.04 eV. This is an additional indication that the pure electronic term gives positive elastoresistance in $\mathrm{WTe_2}$.

8. Theoretical modeling and analysis

To interpret the magneto-elastoresistance (MER) measurements we employ an effective low-energy three-band model. This simplified model can account for the salient features of the ER and the MER, in particular the non-monotonic behavior of ER in zero magnetic field and the increase and rapid saturation of MER as a function of magnetic field. We note that we calculate the elastoresistivity contribution to the elastoresistance, which is given by the first term in Eq. (1), and not the subleading geometric contribution. Our effective model uses as input the strain-induced changes in the electronic band structure, which we infer from experiment and DFT calculations.

The minimal electronic model consists of one hole and one electron band that cross the Fermi energy E_F at $T = 0$ as well as another hole band slightly below E_F (see Fig. 4a). This captures the essence of the band structure of WTe_2 observed by ARPES (6, 19, 20) and first-principle calculations (21) (see also Fig. 3a and Fig. S7) with two pairs of (almost degenerate) electron and two pairs of (almost degenerate) hole bands, and an additional hole band around the Γ point with a flat dispersion (see Fig. S9). Using ARPES, the flat hole pocket was shown to be about 65 meV below E_F (19), which is in good agreement with our DFT calculations, where the heavy-hole pocket appears about 72 meV below E_F. As shown in Fig. S9. there are additional electron pockets slightly above the Fermi energy that we do not include in our effective three-band model. Taking them into account does not change our main qualitative conclusions.

The three bands we consider can be characterized by effective masses m^*_α with $\alpha = e, lh, hh$ corresponding to electron (e), light-hole (lh) and heavy-hole (hh) pockets. We can approximate the effective masses of these bands using SdH oscillation analysis and DFT calculations, neglecting small anisotropies in momentum space. As shown in Table S1, the DFT predicts a ratio of $m^*_{e,\mathrm{DFT}}/m^*_{lh,\mathrm{DFT}} \approx 1/2$. For simplicity and because the precise value does not affect our main conclusions, we set this ratio to unity in our model calculation below: $m^*_e/m^*_{lh} \approx 1$. This is also in agreement with our SdH oscillation analysis (see Fig. 3). It is difficult to extract a precise value for m^*_{hh} from DFT as the band curvature changes relatively quickly as a function of momentum away from the Γ point. We thus set the ratio of $m^*_{hh}/m^*_e = 4.6$ in our low energy model, which qualitatively captures the flatness of the hole band at $E = -72$ meV at the Γ point observed in DFT (see Fig. S9). Again, the precise value does not affect our main conclusions. Let us emphasize that at $T = 0$, results of our simplified model calculation presented below agree with a more detailed DFT transport calculation (see Fig. S8) that takes anisotropies in momentum space properly into account.

Application of uniaxial stress leads to a modification of the bandstructure. At $T = 0$, we can capture this change using DFT calculations, as presented in Fig. S9. Before describing the results, let us emphasize that the numerical DFT results depend on the degree to which correlations are taken into account, and have thus a rather significant degree of variance. In addition, at finite temperatures, other effects such as thermal expansion (under strain) may also play a role. As a result, we use the DFT results as an overall guidance to the strain induced parameter changes in our effective model, but do not constrain ourselves to the exact numerical values predicted by DFT.

At $T = 0$, the changes to the DFT bandstructure induced by compressive strain ($\epsilon_{xx} = -0.2\%$) can to a good approximation be captured by a shift of the bottom (top) of the electron (hole) band and a change of the curvature around the band minima (maxima), corresponding to a change of the carrier's effective masses m^*_α. As shown in Table S1, the two (degenerate) electron bands (labelled 3 and 4) are shifting down in energy by about $\Delta E_{3,4} = -3$ meV (for $\epsilon_{xx} - 0.2\%$), while the two (almost degenerate) hole bands (labelled 1 and 2) shift up by about $\Delta E_1 = 4$ meV and $\Delta E_2 = 6$ meV. Importantly, the heavy-hole band at the Γ point is shifting up by a much larger amount $\Delta E_{hh} = 22$ meV. In our effective three-band model, we take this observation as a qualitative input, but quantitatively differ from the DFT values in Fig. 4 by a factor of five in $\Delta E_{hh}/\Delta E_e$.

The effective masses are also modified by the presence of uniaxial stress. From quantum oscillations we infer that all masses increase under compressive strain with slightly different but comparable rates (see Fig. 3(f)). In contrast, within DFT m^*_{lh} slightly increase and m^*_e slightly decrease (see Table S1). In our model calculation below, we describe a physical mechanism that can explain the non-monotonic behavior of ER from a strain induced change of the carrier density alone. The discrepancy between the change of m^*_α within DFT and quantum oscillation therefore does not affect our main qualitative conclusions, but certainly adds quantitatively to the ER in our experiment. As the masses increase under compressive strain, this adds a negative contribution to the ER (see Eq. (12) below).

A. Elastoresistivity in zero magnetic field. Let us first discuss the case of zero magnetic field $\mathbf{B} = 0$. Using a semiclassical Drude-Boltzmann approach and within the quadratic band approximation, one arrives at the well-known Drude formula for the conductivity $\sigma_\alpha = n_\alpha e^2/(\Gamma_\alpha m^*_\alpha)$, where n_α is the carrier density and Γ_α is the scattering rate of band α. Contributions from different bands add in parallel $\sigma = \sum_\alpha \sigma_\alpha$ and the total resistivity is given by $\rho = \sigma^{-1}$. The elastoresistivity is now governed by a sum of different contributions

$$\frac{1}{\rho(0)}\frac{d\rho(0)}{d\varepsilon_{xx}} = \sum_\alpha \frac{\sigma_\alpha(0)}{\sigma(0)}\left[\frac{\zeta^{(\alpha)}_m}{m^*_\alpha} + \frac{\zeta^{(\alpha)}_\Gamma}{\Gamma_\alpha} - \frac{\zeta^{(\alpha)}_n}{n_\alpha}\right] = \sum_\alpha \frac{\sigma_\alpha(0)}{\sigma(0)}\left[-\frac{\zeta^{(\alpha)}_\mu}{\mu_\alpha} - \frac{\zeta^{(\alpha)}_n}{n_\alpha}\right], \qquad [12]$$

where $\rho(0) \equiv \rho(\mathbf{B} = 0)$, $\sigma(0) \equiv \sigma(\mathbf{B} = 0)$ and we have introduced the strain derivatives $\zeta^{(\alpha)}_m = \frac{dm^*_\alpha}{d\varepsilon_{xx}}$, $\zeta^{(\alpha)}_\Gamma = \frac{d\Gamma_\alpha}{d\varepsilon_{xx}}$ and $\zeta^{(\alpha)}_n = \frac{dn_\alpha}{d\varepsilon_{xx}}$. We also used that the mobility of band α reads $\mu_\alpha = e/(m^*_\alpha\Gamma_\alpha)$. Increasing m^*_α and Γ_α increases the mobility μ_α and the resistivity ρ. On the other hand, increasing the carrier density n_α reduces ρ. Contributions from different bands are weighted according to their contribution to the total conductivity.

To make progress and estimate $d\Gamma_\alpha/d\varepsilon_{xx}$, we will use the scattering rates derived within Boltzmann theory and relate $d\Gamma_\alpha/d\varepsilon_{xx}$ to changes in the density of states and the phonon properties. The scattering rate consists of a temperature T-independent impurity part and a T-dependent phonon part due to scattering off (mainly acoustic) phonons. One finds (22)

$$\frac{1}{\Gamma^{(\alpha)}_{\text{imp}}}\frac{d\Gamma^{(\alpha)}_{\text{imp}}}{d\varepsilon_{xx}} = \frac{\zeta_m^{(\alpha)}}{m^*_\alpha} + \frac{1}{3}\frac{\zeta_n^{(\alpha)}}{n_\alpha} \qquad [13]$$

$$\frac{1}{\Gamma^{(\alpha)}_{\text{ph}}}\frac{d\Gamma^{(\alpha)}_{\text{ph}}}{d\varepsilon_{xx}} = -\frac{\zeta_m^{(\alpha)}}{m^*_\alpha} - 4\frac{\zeta_c}{c_s}\,, \qquad [14]$$

where $\zeta_c = \frac{dc_s}{d\varepsilon_{xx}}$ is the strain induced change of the phonon velocity. More generally, strain may affect $\Gamma^{(\alpha)}_{\text{ph}}$ in a more complicated way, for example, by modifications of the phonon polarization. Under compressive strain, one generally expects that the acoustic phonon velocity increases (hardening) such that $\zeta_c < 0$, due to a change of the Young modulus under strain. As this is a higher order effect in the strain, we expect it to be subleading compared to the change of the carrier densities $\zeta_n^{(\alpha)}$ and the effective masses $\zeta_m^{(\alpha)}$. In Eqs. (13) and (14) we have assumed parabolic and isotropic bands. A more realistic estimate of the strain induced change, in particular of the electron-phonon scattering rate, requires detailed modeling beyond our current work. One can therefore consider $\frac{d\Gamma^{(\alpha)}_{\text{ph}}}{d\varepsilon_{xx}}$ as a phenomenological parameter of our theory. Using the Matthiessen rule, the total scattering rate is given by $\Gamma_\alpha = \Gamma^{(\alpha)}_{\text{imp}} + \Gamma^{(\alpha)}_{\text{ph}}]$, which yields the elastoresistitivy in zero field as

$$\frac{1}{\rho(0)}\frac{d\rho(0)}{d\varepsilon_{xx}} = \sum_\alpha \frac{\sigma_\alpha(0)}{\sigma(0)}\left[\frac{\zeta_m^{(\alpha)}}{m^*_\alpha}\left(1+\frac{\Gamma^{(\alpha)}_{\text{imp}}-\Gamma^{(\alpha)}_{\text{ph}}}{\Gamma_\alpha}\right) + \frac{\zeta_n^{(\alpha)}}{n_\alpha}\left(\frac{1}{3}\frac{\Gamma^{(\alpha)}_{\text{imp}}}{\Gamma_\alpha}-1\right) - 4\frac{\zeta_c}{c_s}\frac{\Gamma^{(\alpha)}_{\text{ph}}}{\Gamma_\alpha}\right]. \qquad [15]$$

A.1. Low-temperature elastoresistivity. At low temperatures phonon scattering is negligible, $\Gamma^{(\alpha)}_{\text{ph}} \ll \Gamma^{(\alpha)}_{\text{imp}}$, and the elastoresistivity is determined solely by electronic terms and bands that cross the Fermi energy. The behavior of the hole pocket below E_F is thus not relevant to the strain response at low temperature, assuming it is not lifted above E_F. Equation (15) therefore simplifies at low T to

$$\frac{1}{\rho(0)}\frac{d\rho(0)}{d\varepsilon_{xx}} = 2\sum_\alpha \frac{\sigma_\alpha}{\sigma}\left(\frac{\zeta_m^{(\alpha)}}{m^*_\alpha} - \frac{1}{3}\frac{\zeta_n^{(\alpha)}}{n_\alpha}\right) \qquad [16]$$

From the analysis of the quantum oscillations, we find that both strain derivatives have the same sign $\zeta_m^{(\alpha)}, \zeta_n^{(\alpha)} < 0$ such that the two effects compete with each other. Which of the two dominates depends on microscopic details. In Fig. 1c, we find that the sign of the elastoresistance in the low temperature regime is different for different samples, while the magnitude rapidly decreases at low T (see Fig. 1). We can understand the increase of the carrier density ($\zeta_n^{(\alpha)} < 0$) within our effective three-band model description by noticing that both DFT and SdH oscillation analysis yield that the hole bands are pulled up in energy by strain, while the electron band is lowered. As we do not find additional SdH frequencies under strain, the heavy hole band remains below E_F even for finite strain. As a result of the band shifts, some electrons are being redistributed from the light hole to the electron band, which increases the total number of carriers $n = n_e + n_h$. Note that the difference of electrons and holes $\Delta n = n_e - n_h$ remains fixed. As described in detail below in Sec. A.3, we thus find a positive contribution to the elastoresistivity from ζ_n within our model (see Fig. 4d at low temperatures).

From the data in Fig. 3e and f, we find that $\zeta_n^{(\alpha)}$ and $\zeta_m^{(\alpha)}$ are of the same order of magnitude. It is therefore difficult to estimate which dominates and unambigously predict the sign. In fact, from a quantitative analysis of our SdH results we estimate that the strain-induced enhancement of the mass slightly dominates, which yields $\frac{1}{\rho(0)}\frac{d\rho(0)}{d\varepsilon_{xx}} < 0$. One should keep in mind, however, that quantum oscillations measure the cyclotron mass, which is a property of an extremal orbit, and not the effective mass $1/m^*_i = \frac{\partial^2 E_{\boldsymbol{k}}}{\partial k_i \partial k_i}$ (or rather the velocity $v_i = \frac{\partial E_{\boldsymbol{k}}}{\partial k_i}$) in the current direction i (averaged over the Fermi surface), which is the quantity relevant for transport (22). In fact, a more detailed microscopic DFT transport calculation predicts a positive slope for ρ/τ, where $1/\tau = \Gamma$, in agreement with experiment. The DFT analysis, however, neglects strain-induced changes in the scattering time τ.

A.2. Intermediate temperature elastoresistivity. At higher temperatures, one must take into account not only the strain-induced modifications of the bandstructure right at the chemical potential $\mu(T)$, but also further away from it within a range of $k_B T$. Strain also affects the carriers in thermally (de)populated bands. This is the dominant effect in semiconductors, where strain leads to a redistribution of carriers among valleys with different effective masses, leading to a characteristic $1/T$ behavior of the elastoresistance (23). We indeed find such a $1/T$ dependence of the elastoresistance at high temperatures $T \gtrsim 250$ K. However, in WTe_2 the behavior is much richer due to the presence of both electron and hole carriers.

The observed increase of the resistivity under compressive strain $\frac{1}{\rho(0)}\frac{d\rho(0)}{d\varepsilon_{xx}} < 0$ at intermediate and high T in Fig. 1c, corresponds to $\zeta_n^{(\alpha)} > 0$, i.e., a decrease in the carrier density under compressive strain. As shown in Fig. 4 and explained in detail in the next section A.3 our three-band model calculation reproduces such a behavior (at intermediate temperatures) using the rigid band energy shift trends under strain obtained from DFT as input (see Fig. 3a and Fig. 4c). The non-monotonic behavior of the elastoresistivity as a function of temperature arises within our model from the fact that the heavy-hole pocket contributes to transport only at finite T, where it is partially filled. Within DFT, strain lifts this pocket up in energy by an amount ΔE_{hh} that is about two times larger than the shifts ΔE_{lh} and ΔE_e found for the other two pockets. As a result, the dominant effect is a redistribution of holes from the light to the heavy hole pocket, resulting in an increase of ρ at intermediate temperatures. The decrease of the number of light holes under strain occurs above a characteristic temperature $k_B T \approx |\mu - E_{hh}(\varepsilon_{xx})|$ (see inset of Fig. 4c), which depends on the shift $\Delta E_{hh} = E_{hh}(\varepsilon_{xx} = -0.2\%) - E_{hh}(\varepsilon_{xx} = 0)$ and the initial distance of the band edge to the chemical potential μ: $|\mu - E_{hh}(\varepsilon_{xx} = 0)|$. We note that the effective mass enhancement observed within quantum oscillations, corresponding to $\zeta_m^{(\alpha)} < 0$, adds with the same sign to the $\zeta_n^{(\alpha)}$ term, making the elastoresistance more negative.

A.3. Details about the low-energy model calculations. Let us now describe in detail the calculation performed within the effective low-energy three-band model that yields the results in Fig. 4. We consider the bandstructure shown in Fig. 4(a), which describes three parabolic bands with energies $E_\alpha(\boldsymbol{k}) = \pm \boldsymbol{k}^2/(2m^*_\alpha) - E_\alpha^{\min}$. Here, the + sign is chosen for the electron band $\alpha = e$ and the − is chosen for the two hole bands $\alpha = lh, hh$. Using input from DFT, we choose the following numerical values for the effective masses $m_e^* = m_{lh}^* = 0.22 m_{hh}^*$ and band energy minima $E_{lh}^{\min} = E_{hh}^{\min} = 0$ and $E_e^{\min} = 0.5$ in the absence of strain. The bands are assumed to have a bandwidth of $W_{lh} = W_e = 1$ and $W_{hh} = 0.5$. We note that this corresponds to the top of the hole bands being located at $E_{lh}^{\max} = E_{lh}^{\min} + W_{lh} = 1$ and $E_{hh}^{\max} = E_{hh}^{\min} + W_{hh} = 0.5$. These values for the band edges and widths leads for the appropriate electron filling to a Fermi surface topology that agrees with the one found within DFT and ARPES. Since the almost perfect compensation of carriers does not play a role in the effect we describe, we do not fine tune the parameters to be in that regime. Note that we set $m_e^*/m_{ls}^* = 1$ for simplicity, which agrees well with our SdH oscillation analysis but deviates from the value of 1/2 found within DFT.

The density of states for the respective bands in three-dimensions reads

$$g_{lh}(E) = \frac{\sqrt{2}(m_{lh}^*)^{3/2}}{\pi^2}\sqrt{W_{lh} - E} \tag{17}$$

$$g_e(E) = \frac{\sqrt{2}(m_e^*)^{3/2}}{\pi^2}\sqrt{E - E_e^{\min}} \tag{18}$$

$$g_{hh}(E) = \frac{\sqrt{2}(m_{hh}^*)^{3/2}}{\pi^2}\sqrt{W_{hh} + E_{hh}^{\min} - E} \tag{19}$$

with energies $E_\alpha^{\min} \le E \le E_\alpha^{\min} + W_\alpha$. We choose a total electronic filling fraction of $n_{\mathrm{el}} = 0.77$, which corresponds to a chemical potential at zero temperature of $\mu(T = 0) = 0.56\, W_{lh}$, shown as the dashed vertical line in Fig. 4(b). This is chosen to result in a Fermi surface topology consistent DFT and ARPES. As noted above, the almost perfect compensation of the number of electrons and holes is not important in our model to reproduce the experimental behavior and we therefore do not fine tune the parameters to correspond to this regime. Note that the heavy-hole band lies below the chemical potential, so the $T = 0$ Fermi surface consists of one hole and one electron pocket. The chemical potential increases as a function of temperature and reaches a value of $\mu(T = 0.1 W_{lh}) = 0.63\, W_{lh}$. Here and in the following we express all energies in units of the light-hole bandwidth W_{lh}.

The application of strain is modelled as rigid band shifts

$$E_\alpha^{\min}(\varepsilon_{xx}) = E_\alpha^{\min}(\varepsilon_{xx} = 0) + \Delta E_\alpha(\varepsilon_{xx})\,. \tag{20}$$

Drawing upon our DFT results, we assume that the electron band is lowered in energy, while the two hole bands shift up. As only relative energy shifts matter, we measure energy shifts with respect to the light-hole band, and use the following parameters $\Delta E_{lh} = 0$, $\Delta E_e = -4 \times 10^{-3} W_{lh}$ and $\Delta E_{hh} = 4 \times 10^{-2} W_{lh}$ for a particular strain value ε_{xx}. By assuming that these rigid band shifts are caused by the experimental strain value of $\varepsilon_{xx} = -0.2\%$ and by comparison to DFT, we can express the light-hole bandwidth energy scale in eV as $W_{lh} \simeq 0.4$ eV. This follows from our findings in DFT that $\Delta E_{hh}(\varepsilon_{xx} = -0.2\%) \approx 16$ meV, , relative to the shift of the light-hole pocket, (see Fig. S9) and thus $W_{lh} = 16$ meV/0.04 = 0.4 eV. Room temperature thus roughly corresponds to 300 K $\simeq 0.06\, W_{lh}$. We note that the ratio of the band shifts $\Delta E_{hh}/\Delta E_e$ we use are about five times larger than the DFT prediction. Importantly, the qualitative outcomes of our calculation are robust to choosing smaller shift values. In particular, the non-monotonic behavior of ER also occurs for shifts that are equal to the DFT predictions, as long as the final position of the hh band is within a range of $k_B T$ of the chemical potential $\mu(T)$. In this case, however, the ER may not experience a sign change that could be attributed to the ζ_n contribution alone, as the ER value at $T = 0$ is too large. In order to reproduce the sign change of ER for these smaller shifts, we would have to invoke contributions arising from the strain-induced change of effective masses ζ_m, which we find to be negative from experiment at low temperatures.

We now demonstrate that one can obtain a non-monotonic behavior of ER as a function of T from the temperature dependence of the strain induced change of the carrier density $\zeta_n(T)$ in Eq. (12) alone. The elastoresistivity $\frac{1}{\rho(0)}\frac{d\rho(0)}{d\varepsilon_{xx}}$ is calculated starting from Eq. (12). Focusing on the ζ_n term, we first need to calculate the number of carriers in the respective bands n_α as a function of temperature T:

$$n_{\alpha \in \{lh,hh\}}(T) = \int_0^{W_\alpha + E_\alpha^{\min}} dE\, g_\alpha(E)\left[1 - n_F(E,T,\mu)\right] \tag{21}$$

$$n_e(T) = \int_0^{W_e + E_e^{\min}} dE\, g_e(E) n_F(E,T,\mu)\,. \tag{22}$$

Here, n_F is the Fermi function. The results for the carrier densities $n_\alpha(T)$ as a function of temperature with and without strain are shown in Fig. 4(c). The contribution of the change of carrier densities to the elastoresistivity for a given value of $\Delta\varepsilon_{xx}$ is then given by (see Eq. (12))

$$\frac{1}{\rho}\frac{\Delta\rho}{\Delta\varepsilon_{xx}}\bigg|_{\zeta_n} = -\sum_\alpha \frac{\sigma_\alpha}{\sigma}\frac{\frac{\Delta n_\alpha}{\Delta\varepsilon_{xx}}}{n_\alpha} = -\sum_\alpha \frac{\frac{\Delta n_\alpha}{\Delta\varepsilon_{xx}}}{n_\alpha + \frac{\Gamma_\alpha}{\Gamma_\beta}\frac{m^*_\alpha}{m^*_\beta} n_\beta + \frac{\Gamma_\alpha}{\Gamma_\gamma}\frac{m^*_\alpha}{m^*_\gamma} n_\gamma} \tag*{[23]}$$

with $\Delta n_\alpha = n_\alpha(\varepsilon_{xx} \neq 0) - n_\alpha(0)$ and $\alpha \neq \beta \neq \gamma$. For simplicity, we use $\Gamma_\alpha/\Gamma_\beta = m^*_\alpha/m^*_\beta$, which holds if impurity scattering is dominant (22) and approximates the ratio of Fermi velocities by $v_F^{(\alpha)}/v_F^{(\beta)} \approx m^*_\beta/m^*_\alpha$. Using the carrier densities $n_\alpha(T)$ and the change in the carrier densities $\Delta n_\alpha(T)$ due to strain ε_{xx} shown in Fig. 4(c), we obtain $\frac{1}{\rho}\frac{\Delta\rho}{\Delta\varepsilon_{xx}}\Big|_{\zeta_n}$ shown in Fig. 4(d). We emphasize again that we use $\Delta\varepsilon_{xx} = -0.2\%$ in the calculation.

Let us now turn to the results of our model calculations. At $T = 0$, we observe that $n_{hh} = 0$ both with and without strain, because the hh band remains below E_F. Electrons solely move from the lh to the e band, resulting in an increase of both electron and hole carrier densities $\Delta n_e > 0$ and $\Delta n_{lh} > 0$. Note that n_α refers to the number of carriers in band α, which corresponds to electrons for $\alpha = e$ and to holes for $\alpha = lh, hh$. Due to the increase in carrier density, the resisitivity is decreasing under the rigid band shift we consider. As this is caused by compressive strain $\varepsilon_{xx} < 0$, the ER, which is a slope, is therefore positive. This description remains valid at low temperatures as long as $k_B T < |\mu - E_{hh}(\varepsilon_{xx})|$, where μ is the chemical potential.

As the temperature increases beyond that value, the behavior of ER changes as the hh band energy E_{hh} is shifted to within a range of $k_B T$ of the chemical potential: $k_B T \approx |E_{hh}(\varepsilon_x x) - \mu|$. This occurs at a characteristic temperature $T_{hh} \approx 0.01 W_{lh}$ for the parameters we have chosen (see inset of Fig. 4(c)). Above this temperature, we find that the hh band is populated by holes in the presence of strain $n_{hh}(\varepsilon_{xx} = -0.2\%, T > T_{hh}) > 0$. As the hh band is flat and its density of states is much larger than the one of the lh band, $g_{hh} > g_{lh}$, holes will move from the lh to the hh band and $\Delta n_{lh} < 0$ for $T > T_{hh}$ (see inset of Fig. 4(c)). As a result the ER will decrease and eventually change sign. This occurs because in the expression for the ER in Eq. (23) the change of carrier density Δn_α is weighted by the individual conductivity of the carrier type σ_α (see middle equation). Due to the large effective mass of the hh carriers, σ_{hh} is small and even though n_{hh} increases due to strain, the effect on the resistivity is small. Instead, the dominant effect on the resistivity is that $\Delta n_{lh} < 0$, which results in a decrease of ER. This effect competes with the increase of $\Delta n_e > 0$, which occurs due to the lowering of the e band by strain and the resulting flow of electrons from the lh to the e band. This increase of e carriers continues to contribute positively to ER, but as shown in Fig. 4(d) this contribution is smaller than the negative one arising from $\Delta n_{lh} < 0$ as long $|\sigma_{lh}\Delta n_{lh}/n_{lh}| > |\sigma_e \Delta n_e/n_e|$. Importantly, we associate this non-monotonic behavior of $\Delta n_{lh}(T)$ as a function of T as the main origin of the non-monotonic behavior of ER that we observe experimentally. Finally, let us emphasize that our model calculations yield a non-monotonic behavior of ER within the range $0 < T/W_{lh} < 0.06$ (see Fig. 4(d)), which corresponds to the range between $T = 0$ and room temperature $T \approx 300$ K. This agrees with the temperature range, where this phenomenon is observed experimentally.

B. Elastoresistance in finite magnetic field. Let us now turn to the analysis of the magneto-elastoresistance (MER), i.e., the elastoresistance in finite magnetic field:

$$\mathrm{MER}(T,B) \equiv \frac{1}{R(T,B,\varepsilon_{xx}=0)}\frac{d[\Delta R(T,B,\varepsilon_{xx})]}{d\varepsilon_{xx}}\bigg|_{\varepsilon_{xx}=0}, \tag*{[24]}$$

where $\Delta R = R(\varepsilon_{xx}) - R(\varepsilon_{xx} = 0)$. Experimentally, as shown in Fig. 2, we observe a rich behavior that can be described as follows: at high temperatures, where the magnetoresistance (MR) vanishes, the magneto-elastoresistance (MER) follows the zero-field elastoresistance (ER). At lower T, when the (non-saturating) MR first becomes finite and then exceptionally large, we find an increase of the MER proportional to B^2 (at small B fields). At temperatures $T \lesssim 50$ K, the observed increase of MER as a function of B crosses over into saturation at a positive plateau value. The saturation value of MER and the saturation field strength B_1 both increase as the temperature is lowered. As we show below, the saturation field scale B_1 can be associated with the coefficient of the quadratic B-field dependence of the non-saturating MR, and our findings of B_1 are in agreement with previous MR measurements. At the lowest temperatures $T < 10$ K, where MR exhibits SdH oscillations, the MER exhibits a delicate and strong dependence on the magnetic field, ranging from $\mathrm{MER}(T_0, B) = +120$ to $\mathrm{MER}(T_0, B') = -80$ in the field range of less than one Tesla: $|B - B'| \approx 0.5$ T (see Fig. 2).

B.1. MER in quantum regime at low temperatures. The interesting behavior of MER quantum oscillations in the quantum regime can be straightforwardly understood from the strain-induced change of the SdH oscillation frequencies that we have experimentally observed. It occurs due to change in size of the extremal orbits (see Sec. 4 in the SI for more details). We find that the orbits increase under compressive strain, which is in agreement with predictions of the three-band model using ΔE_α from DFT as input. Incresing orbits correspond to an increase of carrier densities at low temperatures. At fixed temperature and field, strain can move the minima and maxima of the oscillating resistance such that a position close to the maximum of a SdH oscillation in zero strain becomes a position close to a minimum. This results in a large change of the resistance (see Fig S3). The reverse situation can occur at nearby B-field values, which explains the sign change of $\Delta R_{\varepsilon_{xx},B}$ when B is tuned over a small range.

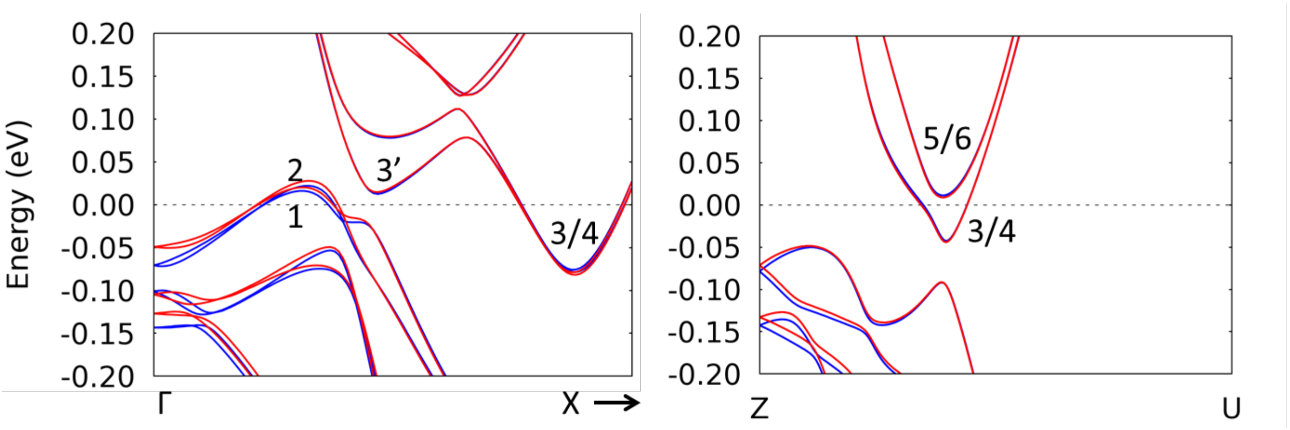

Fig. S9. DFT calculation of band structures DFT band structure for strain (ε_{xx}) at 0 (blue line) and -0.2 % (red line) along Γ-X and Z-U. Band 1 and 2 are the hole bands and band 3 and 4 are the electron bands in Fig. 3. Another set of electron bands (5 and 6) along Z-U are also close to Fermi level. The label i/j means the and i and j overlap with each other and have the same dispersion in the specific pocket region. The label i' means the second pocket region is also of interest because it is near the Fermi level.

Table S1. DFT results of curvature and edge for each band in the pocket regions fitted to parabolics (see numeric label in Fig. S9). The curvature of band 1, 2 and 3/4 along $\Gamma - X$ are the inverse of effective mass for lh and e. In the low-energy model, we set these two effective masses to be approximately equal for simplifty.

Curvature (eV A^2)	1	2	3’	3/4	5/6
ε_{xx} = 0.0 %	-18.4	-19.2	26.6	35.8	15.1
ε_{xx} = -0.2 %	-16.9	-18.2	28.1	37.1	15.4
Edge (eV)	1	2	3’	3/4	5/6
ε_{xx} = 0.0 %	0.028	0.033	0.024	-0.068	0.012
ε_{xx} = -0.2 %	0.032	0.039	0.026	-0.071	0.010

B.2. MER in semiclassical regime at intermediate temperatures. We will now show that the observations in the intermediate temperature regime 10 K $< T <$ 200 K can be qualitatively captured within a semiclassical two-band model description (25) of electron and hole carriers, where the resistivity takes the well-known form

$$\rho(B) = \rho(0)\frac{1 + e\rho(0)(n_e\mu_h + n_h\mu_e)\mu_e\mu_h B^2}{1 + [e\rho(0)\mu_e\mu_h(n_e - n_h)B]^2} = \rho(0)\frac{1 + (B/B_1)^2}{1 + (B/B_{\text{sat}})^2}\,. \tag{25}$$

As above, the zero field resistivity is given by $\rho(0) \equiv \rho(B=0) = \left(\sum_\alpha \sigma_\alpha\right)^{-1}$ with conductivities $\sigma_\alpha = e n_\alpha \mu_\alpha$. The mobilities read $\mu_\alpha = e/(m^*_\alpha \Gamma_\alpha)$ and we have defined the characteristic magnetic field strengths

$$B_1 = [e\rho(0)(n_e\mu_h + n_h\mu_e)\mu_e\mu_h]^{-1/2} \tag{26}$$

$$B_{\text{sat}} = (e\rho(0)\mu_e\mu_h|n_e - n_h|)^{-1}\,. \tag{27}$$

It was shown in previous studies that the carrier compensation in WTe$_2$ is almost perfect and $\Delta n = n_e - n_h$ is very small (26). As a result, MR exhibits purely quadratic dependence on magnetic field with no signs of saturation. The magnetic field range we consider $B <$ 14 T therefore lies in the “intermediate” field regime with $B_1(T) < B < B_{\text{sat}}(T)$.

Starting from Eq. (25) the difference between the elastoresistance at finite and zero magnetic field can be calculated to

$$\Delta\text{MER} \equiv \frac{1}{\rho(B)}\frac{d\rho(B)}{d\varepsilon_{xx}} - \frac{1}{\rho(0)}\frac{d\rho(0)}{d\varepsilon_{xx}} = -\frac{2(B/B_1)^2}{1+(B/B_1)^2}\frac{1}{B_1}\frac{dB_1}{d\varepsilon_{xx}} + \frac{2(B/B_{\text{sat}})^2}{1+(B/B_{\text{sat}})^2}\frac{1}{B_{\text{sat}}}\frac{dB_{\text{sat}}}{d\varepsilon_{xx}}\,. \tag{28}$$

For small magnetic fields, ΔMER varies quadratically with field and reaches a (first) saturation plateau when $B \gtrsim B_1$. The sign of the quadratic dependence and of the saturation plateau depend on the strain derivative of B_1. Experimentally, we observe an in increase of ΔMER with field and a positive saturation value, corresponding to $dB_1/d\varepsilon_{xx} > 0$. At higher fields, $B \approx B_{\text{sat}}$, ΔMER is predicted to vary quadratically with field again, until it finally reaches a (second) saturation plateau when $B \gg B_{\text{sat}}$. Since B_{sat} in WTe$_2$ is larger than the field strengths that we consider, this regime is inaccessible in our experiment, and we only observe the initial increase and the first saturation plateau.

To relate the strain derivative of the two characteristic field strengths $dB_1/d\varepsilon_{xx}$ and $dB_{\text{sat}}/d\varepsilon_{xx}$ to microscopic parameters,

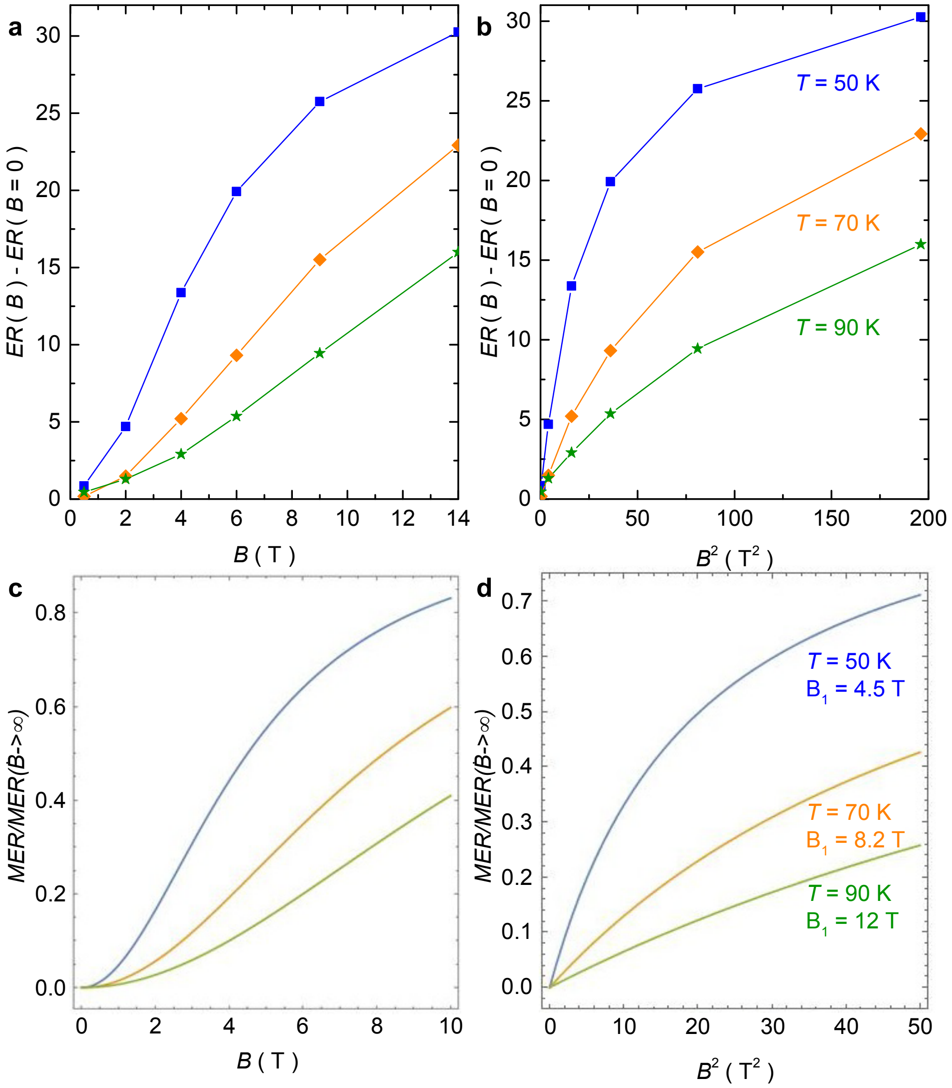

Fig. S10. ΔMER data and simulation a, the magnetic field (B) dependence data of $\Delta\mathrm{MER} \equiv \mathrm{ER}(B) - \mathrm{ER}(0)$ at 50 K (blue), 70 K (orange) and 90 K (green); **b**, the same data as in panel (a) plotted versus B^2 on x-axis; **c**, model prediction for ΔMER using (first term of) Eq. (28). Curves are normalized to their saturation value and value for $B_1(T)$ is extracted from MR data of Ref. (24). Different curves correspond to temperatures of 50 K (blue), 70 K (orange) and 90 K (green); **d** results of panel (c) plotted versus B^2 on x-axis.

we take derivatives of Eqs. (26) and (27) and obtain in the general case

$$\frac{1}{B_1}\frac{dB_1}{d\varepsilon_{xx}} = -\frac{1}{2\rho(0)}\frac{d\rho(0)}{d\varepsilon_{xx}} - \frac{1}{2}B_1^2 e\rho(0)\mu_e\mu_h\left[\left(\frac{\zeta_n^{(e)}}{n_e}+\frac{\zeta_\mu^{(e)}}{\mu_e}+2\frac{\zeta_\mu^{(h)}}{\mu_h}\right)n_e n_h+\left(\frac{\zeta_n^{(h)}}{n_h}+\frac{\zeta_\mu^{(h)}}{\mu_h}+2\frac{\zeta_\mu^{(e)}}{\mu_e}\right)n_h\mu_e\right] \tag*{[29]}$$

$$\frac{1}{B_{\mathrm{sat}}}\frac{dB_{\mathrm{sat}}}{d\varepsilon_{xx}} = -\frac{1}{\rho(0)}\frac{d\rho(0)}{d\varepsilon_{xx}} - \sum_\alpha \frac{\zeta_\mu^{(\alpha)}}{\mu_\alpha} = \sum_\alpha\left[\frac{\sigma_\alpha(0)}{\sigma(0)}\frac{\zeta_n^{(\alpha)}}{n_\alpha} - \frac{\sigma_{\bar\alpha}(0)}{\sigma(0)}\frac{\zeta_\mu^{(\alpha)}}{\mu_\alpha}\right], \tag*{[30]}$$

where $\bar\alpha = e(h)$ for $\alpha = h(e)$. While this general expression for $dB_1/d\varepsilon_{xx}$ in Eq. (29) is complicated, it simplifies considerably under the assumption that electron and hole mobilities are equal $\mu_e \approx \mu_h \equiv \mu$. This assumption is approximately satisfied in $\mathrm{WTe_2}$ (27). Approximating $\mu_e \approx \mu_h \equiv \mu$, one finds

$$\frac{1}{B_1}\frac{dB_1}{d\varepsilon_{xx}} = -\frac{\zeta_\mu}{\mu}\,. \tag*{[31]}$$

An important consequence of this result is that ΔMER directly probes the strain-induced change of the mobility

$$\Delta\mathrm{MER} = \frac{2\zeta_\mu}{\mu}\frac{(B/B_1)^2}{1+(B/B_1)^2} \xrightarrow[B\gg B_1]{} \frac{2\zeta_\mu}{\mu} \tag*{[32]}$$

for $B \ll B_{\mathrm{sat}}$. The saturation value of ΔMER is a direct measurement of ζ_μ/μ under the assumption $\mu_e \approx \mu_h \equiv \mu$. We find that this saturation value is positive for all temperatures, but decrases as temperature is increased. This is in qualitative agreement with an analysis that relies on the previous expressions for $d\Gamma^{(\alpha)}_{\text{imp}}/d\varepsilon_{xx}$ and $d\Gamma^{(\alpha)}_{\text{ph}}/d\varepsilon_{xx}$ in Eqs. (13) and (14) using input from DFT and quantum oscillations that $\zeta^{(\alpha)}_m, \zeta^{(\alpha)}_n < 0$ at low temperatures. We can thus understand the decrease of the saturation value as coming from the increasing importance of phonon scattering, which adds a negative contribution to ζ_μ/μ from the term increase of the phonon velocity under strain $\zeta_c/c_s < 0$.

It is worth emphasizing that the saturation plateau of the MER measures a different combination of strain derivatives as the zero field ER (see Eq. (12)). In particular, it does not explicitly depend on the change of carrier density $\zeta^{(\alpha)}/n_\alpha$. Combining measurements in zero and finite magnetic field thus allows us to gain more insight into the electronic response of the material under strain. Let us discuss one particular example. We find that the saturation value of MER at large fields $B \gg B_1$ is positive for all T, while ER changes sign as a function of T. This contrasting behavior can be traced back to a non-monotonic behavior of the strain-induced change of the carrier densities $\zeta^{(\alpha)}_n$ as a function of T as opposed to $\zeta^{(\alpha)}_m, \zeta^{(\alpha)}_\Gamma$, or $\zeta^{(\alpha)}_\mu$. This follows from the fact that the derivative $\zeta^{(\alpha)}_n$ explicitly only occurs on ER, but not in the saturation value of MER, which measures $\zeta^{(\alpha)}_\mu$.

Finally, we note that at even larger field strengths of $B \gg B_{\text{sat}}$ beyond the regime studied here, the semiclassical analysis predicts that ΔMER reaches another saturation plateau whose value depends on yet another combination of strain derivatives (see Eq. (30))

$$\lim_{B \gg B_{\text{sat}}} \Delta\text{MER} = 2 \sum_\alpha \left[\frac{\sigma_\alpha(0)}{\sigma(0)} \frac{\zeta^{(\alpha)}_n}{n_\alpha} - \frac{\sigma_{\bar\alpha}(0)}{\sigma(0)} \frac{\zeta^{(\alpha)}_\mu}{\mu_\alpha} \right], \qquad [33]$$

where $\bar\alpha = e(h)$ for $\alpha = h(e)$. Interestingly, the strain derivative of the carrier density $\zeta^{(\alpha)}_n$ now occurs with the opposite sign than at zero field, predicting a sign change if this is the dominant effect, as we believe to be the case in WTe_2. Note that in deriving Eq. (33) we have used that the compensation level Δn cannot be tuned by strain due to charge conservation, as long as the quadratic band approximation is valid.

References

1. HH Kuo, MC Shapiro, SC Riggs, IR Fisher, Measurement of the elastoresistivity coefficients of the underdoped iron arsenide $Ba(Fe_{0.975}Co_{0.025})_2As_2$. *Phys. Rev. B* **88**, 085113 (2013).
2. RE Newnham, *Properties of materials: anisotropy, symmetry, structure.* (Oxford University Press on Demand), (2005).
3. JM Gere, *Mechanics of Materials, ; Brooks.* (Cole, Pacific Grove, CA), (2004).
4. F Zeng, WB Zhang, BY Tang, Electronic structures and elastic properties of monolayer and bilayer transition metal dichalcogenides MX_2 (M = Mo, W; X = O, S, Se, Te): A comparative first-principles study. *Chin. Phys B* **24**, 097103 (2015).
5. J Lee, et al., Single- and few-layer WTe_2 and their suspended nanostructures: Raman signatures and nanomechanical resonances. *Nanoscale* **8**, 7854–7860 (2016).
6. Y Wu, et al., Temperature-induced Lifshitz transition in WTe_2. *Phys. Rev. Lett.* **115**, 166602 (2015).
7. DO Brodsky, et al., Strain and vector magnetic field tuning of the anomalous phase in $Sr_3Ru_2O_7$. *Sci. Adv.* **3** (2017).
8. CW Hicks, ME Barber, SD Edkins, DO Brodsky, AP Mackenzie, Piezoelectric-based apparatus for strain tuning. *Rev. Sci. Instruments* **85**, 065003 (2014).
9. P Hohenberg, W Kohn, Inhomogeneous Electron Gas. *Phys. Rev.* **136**, B864–B871 (1964).
10. W Kohn, LJ Sham, Self-Consistent Equations Including Exchange and Correlation Effects. *Phys. Rev.* **140**, A1133–A1138 (1965).
11. BJ Ceperley, D. M.; Alder, Ground-State of the Electron-Gas by a Stochastic Method. *Phys Rev Lett* **45**, 566–569 (1980).
12. A Perdew, J. P.; Zunger, Self-Interaction Correction to Density-Functional Approximations for Many-Electron Systems. *Phys Rev B* **23**, 5048–5079 (1981).
13. A Mar, S Jobic, JA Ibers, Metal-metal vs tellurium-tellurium bonding in WTe_2 and its ternary variants $TaIrTe_4$ and $NbIrTe_4$. *J. Am. Chem. Soc.* **114**, 8963–8971 (1992).
14. SR Rourke, P. M. C.; Julian, Numerical extraction of de Haas-van Alphen frequencies from calculated band energies. *Comput. Phys. Commun.* **183**, 324–332 (2012).
15. GK Madsen, DJ Singh, BoltzTraP. A code for calculating band-structure dependent quantities. *Comput. Phys. Commun.* **175**, 67 – 71 (2006).
16. G Kresse, J Furthmüller, Efficient iterative schemes for ab initio total-energy calculations using a plane-wave basis set. *Phys. Rev. B* **54**, 11169–11186 (1996).
17. PE Blöchl, Projector augmented-wave method. *Phys. Rev. B* **50**, 17953–17979 (1994).
18. HJ Monkhorst, JD Pack, Special points for Brillouin-zone integrations. *Phys. Rev. B* **13**, 5188–5192 (1976).
19. I Pletikosić, MN Ali, AV Fedorov, RJ Cava, T Valla, Electronic Structure Basis for the Extraordinary Magnetoresistance in WTe_2. *Phys. Rev. Lett.* **113**, 216601 (2014).
20. Y Wu, et al., Three-dimensionality of the bulk electronic structure in WTe_2. *Phys. Rev. B* **95**, 195138 (2017).
21. D Di Sante, et al., Three-Dimensional Electronic Structure of the Type-II Weyl Semimetal WTe_2. *Phys. Rev. Lett.* **119**, 026403 (2017).
22. H Smith, HH Jensen, *Transport Phenomena.* (Oxford University Press, Oxford, U.K.), (1989).
23. Y Kanda, Y Kanda, A graphical representation of the piezoresistance coefficients in silicon. *IEEE Transactions on Electron Devices* **29**, 64–70 (1982).

24. MN Ali, et al., Large, non-saturating magnetoresistance in WTe_2. *Nature* **514**, 205–208 (2014).
25. A Pippard, *Magnetoresistance in Metals* eds. A Goldman, P McClintock, M Springford. (Cambridge university press), (1989).
26. MN Ali, et al., Correlation of crystal quality and extreme magnetoresistance of WTe_2. *EPL (Europhysics Letters)* **110**, 67002 (2015).
27. Y Luo, et al., Hall effect in the extremely large magnetoresistance semimetal WTe_2. *Appl. Phys. Lett.* **107**, 182411 (2015).